J. Fluid Mech. (2014), *vol.* 753, *pp.* 472–498. © Cambridge University Press 2014
doi:10.1017/jfm.2014.371

Inertial wave dynamics in a rotating liquid metal

Tobias Vogt†, Dirk Räbiger and Sven Eckert

Institute of Fluid Dynamics, Helmholtz-Zentrum Dresden-Rossendorf (HZDR), PO Box 510119, 01314 Dresden, Germany

(Received 9 September 2013; revised 29 April 2014; accepted 24 June 2014; first published online 25 July 2014)

The dynamics of free and forced inertial waves inside cylinders of different aspect ratios ($A = H_0/2R_0$) were investigated experimentally in this study. The liquid metal GaInSn was chosen as the fluid in order to enable a contactless stimulation of the flow by means of alternating electromagnetic fields. A rotating magnetic field generates the rotating motion of the liquid, whereas periodic modulations of the field strength and short pulses excite specific wave modes. Ultrasound Doppler velocimetry was used to record the flow structure and to identify inertial waves in the set-up. Our experiments demonstrate selective excitation of different inertial wave modes by deliberate variation of the magnetic field parameters. Furthermore, it was found that turbulent perturbations in the boundary layers of the swirling flow are able to induce an inertial wave mode that survives over a long time. Experiments at the fundamental resonance have shown that multiple harmonic wave modes appeared simultaneously. The measured inertial wave frequencies were compared to the predictions of the linear inviscid theory.

Key words: MHD and electrohydrodynamics, wave–turbulence interaction, waves in rotating fluids

1. Introduction

Inertial waves appear to be a ubiquitous feature in rotating fluids, occurring often in both nature and the laboratory. In nature, the Earth's rotation drives very large-scale inertial waves in, for example, the atmosphere (Thompson 1978), oceans (Fu 1980) and the Earth's liquid core (Aldridge & Lumb 1987). Besides this, inertial waves can also be detected in a variety of technical applications. In all cases, the source for an inertial wave is a disorder in the centrifugal force balance of the rotating fluid. Such an imbalance leads to a radial flow and thus to a Coriolis force that acts in the azimuthal direction on radially shifted fluid. The stability of radial flow depends on the radial distribution of the angular momentum in the base flow. If viscous damping is neglected, the stability boundary is given by the Rayleigh (1917) stability criterion:

$$\frac{\partial}{\partial r}(u_\phi r) \geqslant 0. \tag{1.1}$$

If the azimuthal velocity decreases faster than this limit, the centrifugal force and the radial pressure gradient are out of balance and even small disturbances of the flow

† Email address for correspondence: t.vogt@hzdr.de

https://doi.org/10.1017/jfm.2014.371 Published online by Cambridge University Press

field will lead to turbulence. Otherwise, the flow is stable, but capable of oscillation via inertial waves when disturbed appropriately. Kelvin (1880) was the first to study this type of wave mathematically. Later, Bjerknes & Solberg (1929) studied inertial waves mathematically in the context of meteorology. One important finding of theirs is that the frequency of such inertial waves is always less than twice the rotational speed of the basic flow field. This frequency limit can be written as

$$f_{iw} \leqslant \Omega/\pi, \tag{1.2}$$

where f_{iw} is the frequency of the inertial wave and Ω stands for the angular velocity of the rotating fluid. They also developed a set of equations for calculating the eigenperiod of a given wave mode (see § 6). The first experimental study dealing with inertial waves was made by Görtler (1957). He considered small forced oscillations in an incompressible fluid in solid-body rotation inside a rotating Perspex cylinder. A small oscillating plate in the middle of the cylinder forced the inertial waves. He was able to verify the frequency limit predicted by Bjerknes & Solberg (1929) with reflecting aluminium particles suspended in the fluid. The next step was made by Fultz (1959), whose experiments show a remarkably close agreement with the theoretically calculated free periods. In his experiments he also used an oscillating plate to force inertial waves. Manasseh (1992) and Kobine (1995) investigated inertial waves experimentally in a rotating cylinder subject to precessional forcing. In both experiments, a transition to a disordered or turbulent flow was observed when the fluid was forced near a resonant frequency. However, this phenomenon, also known as resonant collapse, appeared less violent in the experiments carried out by Kobine (1995). Kobine concluded that the resonant collapse is caused by nonlinear interaction of various inertial wave modes. Furthermore, his results support the use of the linear inviscid theory in modelling the fluid response under conditions where the forcing is away from the primary resonance, and for short times after the onset of resonant precessional forcing.

Inertial waves remain an active subject of investigation, with many researchers studying their occurrence in various geometries. Messio *et al.* (2008) focused on inertial waves in a rotating cylinder, where the wave modes were generated by a small oscillating disc. Inertial waves have also been studied in rotating spherical shells (see Kelley *et al.* 2007; Baruteau & Rieutord 2013). Kelley *et al.* (2010) attributed the excitation of a Coriolis-restored inertial mode to a critical layer of the mean axisymmetric flow.

The imposition of a DC magnetic field can give rise to hydromagnetic or magneto-Coriolis waves (Schmitt *et al.* 2008). Magnetic fields are also used in our experiment to generate the rotating motion of the liquid metal and to trigger different wave modes. However, it can be easily shown that AC magnetic fields at low field strengths (of the order of a few milliteslas), such as those used in these experiments, induce no magneto-Coriolis waves.

Here we present a new approach for excitation of inertial waves in liquid metal flows. Inertial waves are typically triggered by mechanical agitation – using oscillating plates, librating cylinder walls or feed-ins with oscillating flow rates – and by specific geometric arrangements – including inclined end plates of the rotating cylinder, or inclined cylinders – that cause a precessional flow. In our case, the application of a rotating magnetic field (RMF) exerts a volumetric body force on a liquid metal inside a stationary cylindrical vessel, driving a rotational flow (Davidson & Hunt 1987). Consequently, the experiment presented here exhibits two main differences with

https://doi.org/10.1017/jfm.2014.371 Published online by Cambridge University Press

respect to the classical experiments on inertial waves: (i) the rotating motion in the cylinder at rest implies the permanent existence of boundary layers. A recirculation torus forms in the meridional plane of the vessel due to the Ekman pumping in the developed Bödewadt layers at the top and bottom walls. (ii) The swirling flow field cannot be considered as a solid-body rotation. The velocity falls to zero at the cylinder sidewalls. We will see that the angular velocity shows an almost linear decrease from the cylinder axis towards higher radii. In addition, flow instabilities in the form of Taylor–Görtler (TG) vortices appear in turbulent flows at the sidewall boundary layers of the non-rotating cylinder.

The aim of the present experimental work is to investigate the occurrence and properties of inertial waves in such a complex flow configuration. The excitation of the inertial waves is realized in our experiments either by an unsteady forcing, exerted by a modulation of the RMF strength, or by a perturbation of the flow through short electromagnetic pulses. Flow measurements inside the closed cylindrical liquid metal column were carried out by means of ultrasound Doppler velocimetry (UDV). This study demonstrates that electromagnetic fields can be considered as an effective tool for generating a variety of inertial wave modes in a laboratory-scale set-up. Besides the fundamental interest in the manifestation of inertial waves, such kinds of transient flows may occur in diverse technical applications, such as liquid metal mixing (Eckert *et al.* 2007) or grain refinement in solidification processes (Griffiths & McCartney 1996), where electromagnetic stirring and the use of time-modulated RMF for intermittent stirring is considered for flow control.

2. Magnetic body force and RMF-induced flow

Liquid metal experiments offer an attractive possibility to reproduce large-scale flow phenomena of geo- and astrophysics at laboratory scale (see Gailitis *et al.* 2001; Stieglitz & Müller 2001; Nataf *et al.* 2006; Stefani *et al.* 2006; Kelley *et al.* 2007; Monchaux *et al.* 2007; Grants *et al.* 2008; Vogt *et al.* 2013). In this study we consider the case of a liquid metal in a closed stationary cylinder exposed to an RMF, where the rotational axis of the RMF is axially aligned with the cylinder axis. Various inertial modes are triggered in the liquid metal by either an amplitude-modulated RMF or short magnetic field pulses. Assuming a low field frequency Ω, the skin effect becomes negligible and the magnetic field (B_R) can penetrate completely throughout the liquid metal. This low-frequency condition is satisfied for (Tacke & Schwerdtfeger 1979)

$$S = \mu_0 \sigma \omega R_0^2 < 1, \tag{2.1}$$

where S is the shielding parameter, μ_0 is the magnetic permeability, σ is the electrical conductivity of the liquid metal and R_0 is the vessel radius. Previous studies have shown that this low-frequency approximation gives reasonable results (to within 4 %) up to values of $S \approx 3$ (see Tacke & Schwerdtfeger 1979; Davidson 1992). The magnetic field frequency was fixed during our experiments to $\omega/2\pi = 50$ Hz, yielding a shielding parameter $S = 1.14$, where the impact of the skin effect on the force distribution is insignificant. It is further assumed that the flow does not influence the driving force. This so-called low-induction condition is generally fulfilled if the angular velocity of the fluid is much smaller than the magnetic field frequency. In our case, these frequencies differ by at least a factor of 10. In this low-frequency and low-induction approximation, the Lorentz force is time-independent and has only one azimuthal component in the cylindrical configuration, which can be calculated as follows (Gorbachev, Nikitin & Ustinov 1974):

$$F_\phi = \sigma \omega B_R^2 r f(r, z). \tag{2.2}$$

https://doi.org/10.1017/jfm.2014.371 Published online by Cambridge University Press

The shape function $f(r, z)$ reflects the influence of the finite cylinder length. The Lorentz force has its maximum near the sidewall of the vessel at the half-height and reduces to zero at the axis and the horizontal endwalls. This force drives a primarily swirling flow. However, the velocity distribution of this swirling flow is quite different from a solid-body-like rotation, as we shall see in § 6. The core of the fluid rotates faster than the fluid at higher radii. The velocity at the walls is zero due to the fact that our cylinders are non-rotating. The Ekman transport at the top and bottom walls of the cylinder drives two counter-rotating recirculation tori in the meridional (r, z) plane of the vessel (Davidson 1992). The velocities of this secondary flow are about one order of magnitude lower than the primary rotation of the liquid metal. For a more detailed description of the RMF-driven flow inside stationary cylinders, we refer to Stiller, Fraňa & Cramer (2006). The magnetic Taylor number gives the dimensionless force magnitude that is used to characterize the RMF-driven flow:

$$Ta = \frac{\sigma \omega B_R^2 R_0^4}{\rho \nu^2}. \tag{2.3}$$

The magnetic flux density B_R in (2.3) and (2.2), respectively, is given in terms of the root-mean-square value. A critical Taylor number (Ta^{cr}) can be defined for the transitional force where the laminar RMF-driven flow becomes unstable and transition to turbulence occurs. This critical parameter ranges between values of 1.44×10^6 and 2.26×10^4 for aspect ratios between 0.5 and 2, respectively (Grants & Gerbeth 2002). For the aspect ratio $A = 3$ the critical Taylor number is $Ta^{cr} = 1.37 \times 10^4$ (I. Grants, 2012, personal communication). The range of electromagnetic forcing considered in this work is clearly supercritical, leading to a distinctly turbulent flow ($Ta \approx 10^6$–$10^7 \gg Ta^{cr}$). Previous investigations revealed that the secondary flow in a transient or turbulent regime is dominated by the formation of TG vortices at the sidewall of the vessel (see Grants & Gerbeth 2001; Stiller *et al.* 2006; Räbiger, Eckert & Gerbeth 2010; Vogt *et al.* 2012).

Hydromagnetic or magneto-Coriolis waves appear if strong Lorentz forces are in competition with the inertia forces. Notwithstanding that AC magnetic fields are applied in our experiment, the respective field strengths are of the order of a few milliteslas. This leads to correspondingly low Lundquist, $\mathcal{O}(10^{-2})$, and Elsasser, $\mathcal{O}(10^{-5})$, numbers, which indicates that any direct influence of the Lorentz force on the wave dynamics can be neglected in the present study.

The classification of the different inertial wave modes is done in this work with the waveform vector (γ_i, n, m), where γ_i is the wavenumber of the ith radial mode, n is the axial mode number and m is the azimuthal mode number. The fact that our experimental set-up is entirely axisymmetric (the cylinders as well as the magnetic field) gives rise to the assumption that all inertial wave modes excited in this experiment are also axisymmetric ($m = 0$). Thus, we use only the reduced waveform vector (γ_i, n) for the inertial wave classification throughout this work.

3. Experimental set-up

The flow measurements were conducted in the eutectic alloy $Ga_{68}In_{20}Sn_{12}$, which is liquid at room temperature ($T_{melting} = 10.5\,^{\circ}C$) and has approximately one-third the kinematic viscosity of water. Some selected material properties of the alloy are shown in table 1. The liquid metal was filled into closed cylindrical vessels made of Perspex. Three fluid cylinders were used in this study having an identical inner diameter of

https://doi.org/10.1017/jfm.2014.371 Published online by Cambridge University Press

Property	Symbol	Value	Unit
Density	ρ	6.36×10^3	kg m^{-3}
Viscosity	ν	3.4×10^{-7}	m^2 s^{-1}
Electrical conductivity	σ	3.2×10^6	S m^{-1}

TABLE 1. Material properties of GaInSn at room temperature (297 K).

$D = 2R_0 = 60$ mm and different heights of $H_0 = 60$, 120 and 180 mm, corresponding to aspect ratios of $A = H_0/2R_0$ of 1, 2 and 3, respectively. The fluid vessels were placed concentrically inside the borehole (diameter 350 mm, height 400 mm) of the MULTIpurpose MAGnetic field system (MULTIMAG) at HZDR. MULTIMAG is a compact magnetic coil system for the generation of an RMF, a vertically travelling magnetic field (TMF) and a pulsating magnetic field and superpositions thereof with a high accuracy (Pal *et al.* 2009). A three-phase current generates the RMF inside a radial arrangement of six coils, with opposing coils connected as pole pairs. The magnetic field vector rotates in a horizontal plane. The rotational axes of the magnetic field and fluid cylinder are identical. The TMF is induced inside a line-up of six coils that are fed by a six-phase current. The TMF induces a Lorentz force that acts mainly in the axial direction, unlike the application of the RMF, which creates a force in the azimuthal direction.

Measurements of the fluid velocities were obtained by means of the UDV, which delivers instantaneous velocity profiles along a ray, and is suitable for opaque fluids such as liquid metals (see Takeda 1991; Brito *et al.* 2001; Eckert & Gerbeth 2002; Grants *et al.* 2008). The technique uses short ultrasound bursts emitted from an ultrasound transducer in acoustic contact with the measured flow. The same transducer receives the ultrasound echo reflected from acoustic inhomogeneities inside the fluid. In the case of GaInSn, these inhomogeneities are assumed to be microscopic oxide particles, which inevitably occur in such non-precious liquid metals. Thus, there was no need to add special tracers to the liquid metal. The measurements assume that the reflecting particles are homogeneously dispersed in the melt and follow the flow without slip. The distance between the UDV transducer and the echo-reflecting particle is calculated by the time of flight of the ultrasound burst. The velocity component in the beam direction is calculated by the phase shift of subsequent ultrasound burst echoes. The velocity component perpendicular to the ultrasound beam is not detectable by this technique. A DOP2000 velocimeter (model 2125, Signal Processing SA, Lausanne) was used in the present study. The respective fluid cylinders were equipped with five 8 MHz UDV transducers (TR0805LS, acoustic active diameter 5 mm) at the bottom of the vessel at different radial and azimuthal positions as indicated in figure 1. The front surface of the UDV transducers is in direct contact with the liquid metal in order to ensure sufficient acoustic coupling and good measuring quality even at very low fluid velocities. The measuring line of sensor 1 coincides with the vessel axis. Sensor 2 is placed at $r/R_0 = 0.45$ and the three outer sensors (3, 4 and 5) are located at $r/R_0 = 0.9$ with an angle of 60° between neighbouring sensors. These five sensors measure the vertical velocity distribution in the cylinder along the ultrasound beam, which is parallel to the vessel axis. A sixth UDV transducer was positioned at the half-height of the vessel along a chord at a radial distance of $r_s = 5$ mm for recording the azimuthal velocity component of the liquid metal. The spatial resolution of the ultrasound transducers

https://doi.org/10.1017/jfm.2014.371 Published online by Cambridge University Press

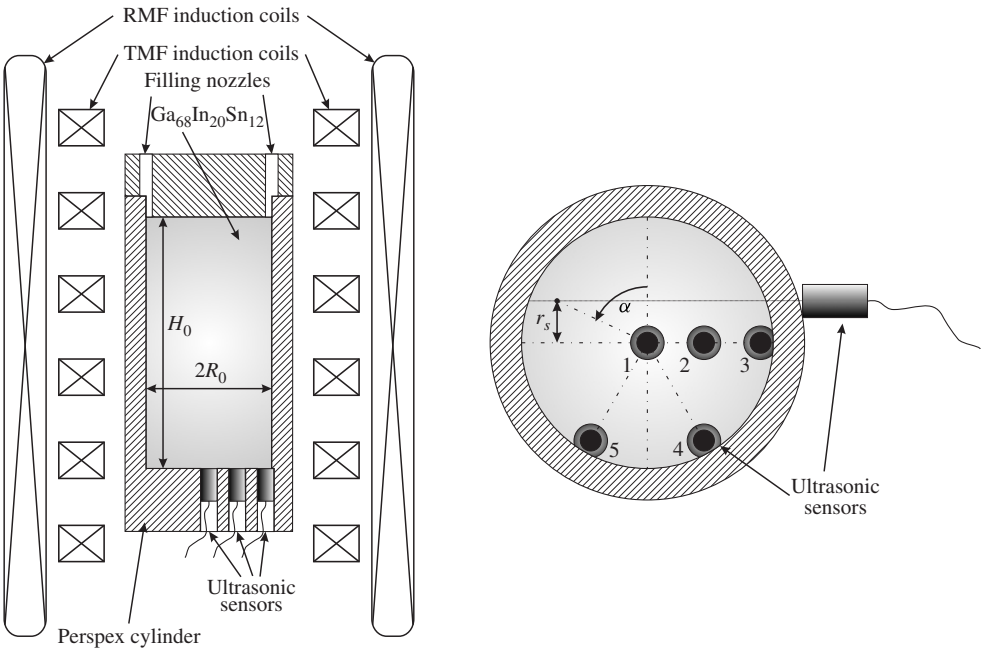


FIGURE 1. Schematic drawing of the experimental set-up and applied sensor positions.

achieved in GaInSn is approximately 1.4 mm in the axial direction and 5 mm in the lateral direction. The latter increases slightly in the measuring direction owing to a divergence of the ultrasound beam of approximately 3°. The temporal resolution of the measuring system is approximately 10 Hz. In order to analyse the flow pattern in more detail, we applied a two-dimensional fast-Fourier transformation (2D-FFT) to the spatio-temporal flow structure recorded at the vessel axis, which here allows for simultaneous frequency and axial wavenumber analysis.

4. Spontaneous occurrence of inertial waves

Inertial waves can be excited in a liquid metal column by variations of the electromagnetic driving force. For instance, pronounced inertial waves were found during an RMF-driven spin-up after the magnetic field had been suddenly switched on (Nikrityuk *et al.* 2005; Räbiger *et al.* 2010). These inertial waves are completely damped by viscous effects before the flow reaches the steady state at the end of the spin-up. Having this in mind, one would hardly expect inertial waves to occur during a stationary rotation without external perturbation. In a recent work, Sauret *et al.* (2005) analysed numerical simulations of the flow in a librating cylinder, and reported a new mechanism of spontaneous excitation of inertial waves in the centre of the cylinder ensuing from turbulent sidewall boundary layers.

To check whether turbulent fluctuations may act as a source of such perturbations, a series of experiments were performed under stationary flow conditions with a continuously rotating liquid, avoiding any geometrical or electromagnetic perturbations. The measurements were performed inside a cylinder with aspect ratio $A = 3$ ($H_0 =$ 180 mm and $R_0 = 30$ mm). The rotating flow inside the cylindrical vessel was driven by an RMF at constant field strength of $B_R = 1.3$ mT, corresponding to a value

https://doi.org/10.1017/jfm.2014.371 Published online by Cambridge University Press

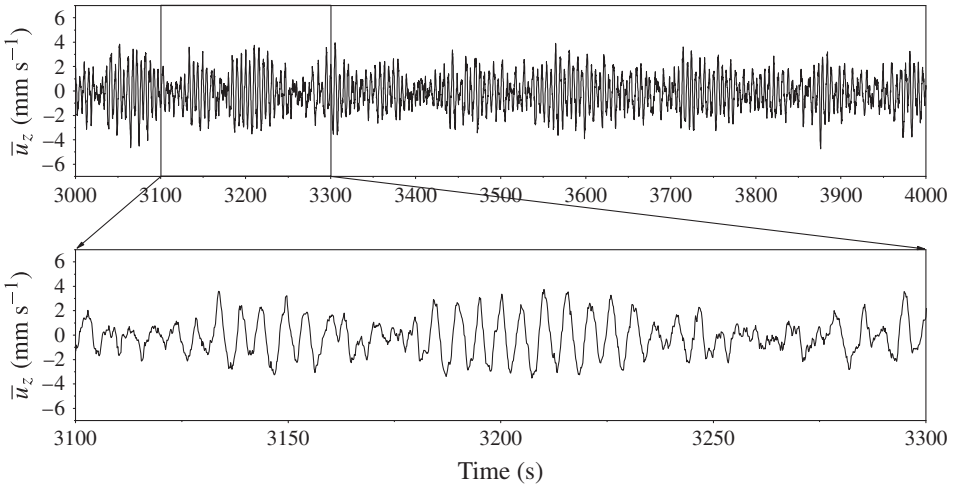


FIGURE 2. Mean axial velocity averaged along the cylinder height, $0 \leqslant z \leqslant H_0$, recorded during a long-term measurement without magnetic disturbance; $B_R = 1.3$ mT; $r/R_0 = 0$.

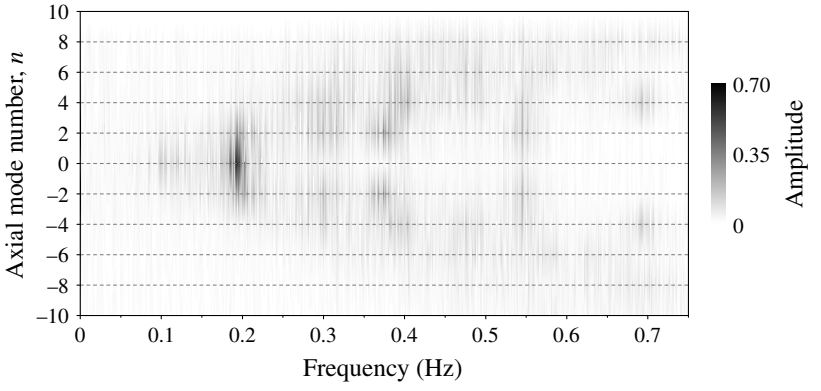


FIGURE 3. The 2D-FFT of the spatio-temporal flow structure recorded during a long-term measurement without magnetic disturbance (corresponds to the measurement shown in figure 2); $B_R = 1.3$ mT; $r/R_0 = 0$.

of the magnetic Taylor number of $Ta = 1.79 \times 10^6 \gg Ta^{cr}$. RMF-driven flows at approximately $100 \times Ta^{cr}$ can be considered as supercritical to certain instabilities.

Figure 2 displays the evolution of the vertical velocity (u_z) averaged along the axis of the liquid metal column in a section of a long-term (∼1 h) measurement. A nearly periodic oscillation of the mean axial velocity becomes visible, collapsing intermittently. Because any external forcing was avoided here, the inertial wave must be triggered by the flow itself. A frequency and wave-mode analysis of this inertial wave was done in terms of a 2D-FFT, shown in figure 3. In this figure, the vertical axis is determined by the axial mode number, defined as $n = 2H_0/\lambda$, where λ is the wavelength. The abscissa represents the frequency. The normalized amplitude of the respective wave modes is represented by the grey scale. This 2D-FFT was performed within the measuring time interval of $t = 3000$–4000 s. The diagram clearly reveals the dominant $(\gamma_1, 1)$ mode with a frequency of $f \approx 0.19$ Hz. Because the wavelength

https://doi.org/10.1017/jfm.2014.371 Published online by Cambridge University Press

of the $n = 1$ inertial wave is twice the cylinder height, the FFT does not identify a complete wave. The mode-number information of the FFT is therefore projected to $n = 0$ (representing a uniform component) and to various positive and negative integer wavelengths (a similar decomposition occurs for all odd modes). The $n = 2$ signature at $f = 0$ Hz, which can be seen in most of the FFT plots that follow, is a signature of the Bödewadt recirculation. Several other inertial wave modes can be identified in this FFT plot in addition to the dominant $(\gamma_1, 1)$ mode, such as the $n = 2$ mode at $f \approx 0.4$ Hz. The interesting question is how these inertial wave modes are excited. A typical feature of an RMF-driven flow at supercritical *Ta* numbers is the formation of TG vortices, which result from the instability of the sidewall layers (Grants & Gerbeth 2002). These TG vortices typically develop in the boundary layer at the sidewall of the cylindrical vessel. After formation, they are conveyed by the secondary flow towards the horizontal endwalls of the vessel, where they dissipate in the Bödewadt layers (Stiller *et al.* 2006). The impingement of the TG vortex on the Bödewadt layer provokes a temporary disturbance of the boundary layer. Velocity measurements made during an RMF-driven spin-up by Vogt *et al.* (2012) showed how such a disturbance propagates inside the boundary layer and excites an inertial wave in the centre of the vessel, as observed in figure 2. These findings suggest that spontaneous generation of inertial waves might be caused by the dissipation of TG vortices in the Bödewadt layers.

With the exception of the $(\gamma_1, 1)$ mode, all inertial waves detected in the velocity measurements do not become prevalent with respect to the turbulent motion. Thus, we will now focus in more detail on the dominant $(\gamma_1, 1)$ mode. Figure 2 demonstrates that the amplitude of $(\gamma_1, 1)$ mode remains more or less stable for many periods, although it intermittently experiences sudden decay. Thus, there must be a mechanism sustaining the $(\gamma_1, 1)$ wave. We ascribe this interesting phenomenon to an interaction between the $(\gamma_1, 1)$ mode and the pronounced Bödewadt layers at the top and bottom walls of the vessel. According to the velocity recordings in figure 2, the inertial wave induces an alternating upwards or downwards directed flow along the vessel axis. This alternating flow leads to periodic variations of the Bödewadt layer thickness and thus to a periodic modulation of the Ekman transport. Let us consider a moment when the inertial wave in the centre of the vessel is directed upwards. At that instant the Ekman transport beneath the lid of the fluid cylinder is repressed, while the liquid metal is still pumped inwards in the bottom Bödewadt layer. As a result, an upwards directed jet is formed in the core of the fluid vessel. A half-cycle later, the situation reverses and a downwards directed jet is formed. This alternating Ekman transport is by necessity in phase with the inertial wave, which suggests that the Ekman transport is continuously transferring energy from the primary swirling flow to the inertial wave. Such a mechanism, though speculative at present, could be responsible for the persistence of the $(\gamma_1, 1)$ inertial mode.

This mechanism would also explain the observations reported by Zhang *et al.* (2011) for the situation of an RMF-driven flow in a liquid metal column, where the free surface of a liquid metal was covered by a distinct oxide layer. In this case an intense distortion of the bulk flow occurred without external stimulation. The authors suggest the friction forces between the rigid oxide layer and the sidewall to be responsible for the development of pronounced flow oscillations in the bulk of the melt. However, they did not associate their findings with the occurrence of inertial waves. A closer analysis of the flow pattern found in the reported experiment and a comparison with the results of the present study reveals the existence of the $(\gamma_1, 1)$ mode in that experiment. The strong interaction between this inertial wave and the oxide layer, which causes strong and persistent flow oscillations, appears to be similar to the mechanism described in this section.

https://doi.org/10.1017/jfm.2014.371 Published online by Cambridge University Press

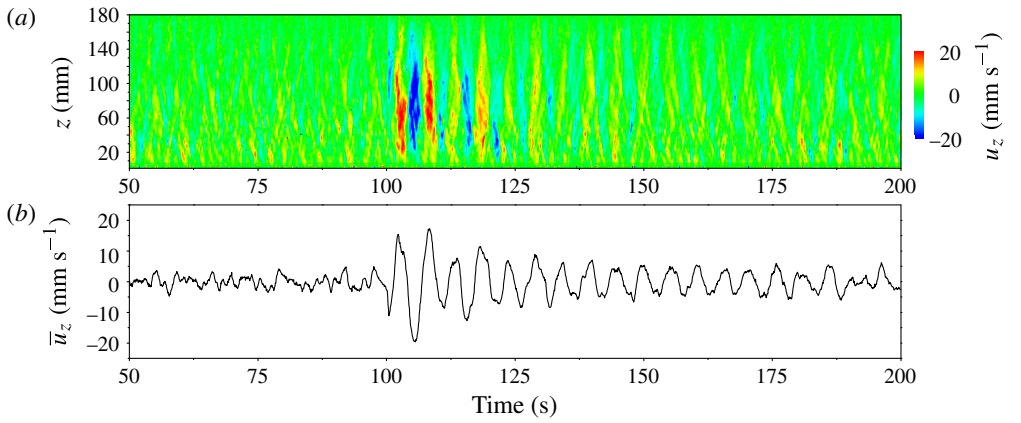


FIGURE 4. Free inertial wave along the axis of the rotating liquid metal column excited by a vertically directed pulse; $B_R = 1.3$ mT. Pulse: $t = 100$ s; $\Delta t_p = 0.2$ s; $B_T = 17.8$ mT. (*a*) Axial velocity at $r/R_0 = 0$; (*b*) mean axial velocity averaged along the cylinder height, $0 \leqslant z \leqslant H_0$.

5. Free inertial waves generated by a short magnetic field pulse

The previous section described the sustained, self-excited inertial waves in a turbulent RMF-driven flow. Two complementary mechanisms were suggested to explain the spontaneous occurrence and the self-preserving behaviour of the $(\gamma_1, 1)$ inertial mode. While the excitation can be related to the dissipation of TG vortices in the Bödewadt layer, the survival of the inertial mode is governed by the reciprocal action of inertial wave and Ekman transport. To study this second mechanism in more detail, further measurements were conducted with the random excitation of inertial wave modes replaced by a well-defined and reproducible impulsive perturbation of the rotating liquid metal flow. In this series of experiments, the rotating flow was exposed to a strong, but very short duration, magnetic field pulse in either a TMF or RMF configuration. These pulses generate a short-time propulsion of the liquid either in the axial direction TMF or in the azimuthal direction RMF. The field strength of each pulse was set significantly higher than that of the RMF that continuously drives the background rotation of the fluid. The time duration of the pulses was chosen to be as short as possible in order to avoid a substantial change of the main rotating flow. Both the TMF and RMF pulses produce free inertial waves, which decay gradually.

5.1. *Vertically directed pulse*

The rotating flow was exposed to a downwards directed TMF pulse ($B_T = 17.8$ mT) for a duration of $\Delta t_p = 0.2$ s. The liquid metal was driven by the same RMF field strength as during the experiments presented in the previous section ($B_R = 1.3$ mT). The RMF was run over a sufficiently long period, lasting for at least three times the spin-up time (Nikrityuk *et al.* 2005), in order to produce a quasi-stationary background rotation before the measurements were started. Figure 4(*a*) shows the spatio-temporal flow structure recorded along the rotational axis of the liquid metal column. The ordinate represents the cylinder height; the abscissa shows the running time of the measurement. The velocity is represented by the colour map. A positive velocity (red) indicates an ascending flow whereas blue (negative values) stands for

https://doi.org/10.1017/jfm.2014.371 Published online by Cambridge University Press

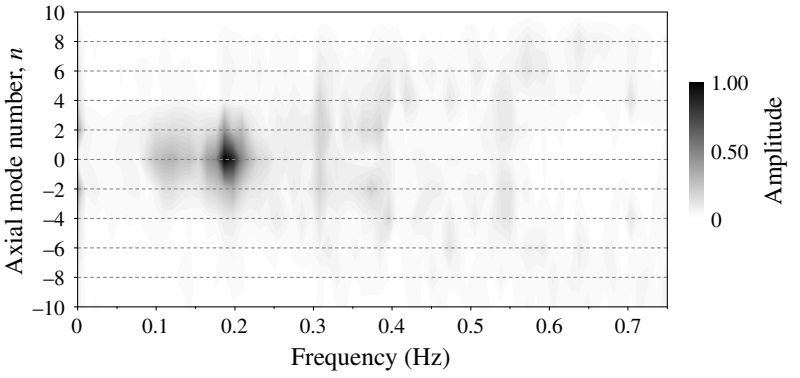


FIGURE 5. The 2D-FFT of the spatio-temporal flow structure excited by the TMF pulse (corresponding to the measurement shown in figure 4*a*). FFT time interval: 100 s $\leqslant t \leqslant$ 190 s.

a descending flow. The short vertical TMF pulse was imposed at the time $t = 100$ s. This creates a free inertial wave with an axial mode number of $n = 1$, which can be detected in both the spatio-temporal velocity plot (figure 4*a*) and the time series of the vertical velocity averaged along the vessel axis (figure 4*b*). This $(\gamma_1, 1)$ wave mode forms one large toroidal vortex ring around the rotational axis that occupies almost the entire fluid volume. The same mode occurred spontaneously, without any external flow perturbation, during the experiments reported in the previous section. The application of the TMF pulse leads to significantly higher intensities of the inertial waves. The comparison of the corresponding 2D-FFTs (figures 3 and 5) reveals identical frequencies for the TMF-triggered inertial wave and the self-excited inertial wave, which is unsurprising, as both measurements were performed at the same RMF field strength and thus at the same rotation rate of the fluid.

The evolution of the amplitudes is shown in figure 4(*b*). Immediately after the short TMF pulse, the mean axial velocity reaches a maximum amplitude of $\hat{u} \approx \pm 20$ mm s^{-1}. The amplitude is supposed to decay exponentially towards zero due to viscous effects as reported by Kobine (1995). However, the decay rate of the inertial wave here looks different. After an initial decay of the amplitudes, a long interval appears while the amplitude remains at a constant level of $\hat{u} \approx \pm 5$ mm s^{-1}. This finding confirms the suggestion of the previous section that a long-term stability of the $(\gamma_1, 1)$ wave mode might be supported by the interaction with the Bödewadt layers.

5.2. *Azimuthally directed pulse*

We now consider the case where the flow field of the rotating liquid metal is disturbed by a positive, azimuthally directed acceleration excited by an RMF pulse. The background rotation is the same as chosen in § 5.1 ($B_R = 1.3$ mT). The spatio-temporal flow structure at the vessel axis in figure 6(*a*) shows the resultant inertial wave, assigned to the axial mode number of $n = 2$. The 2D-FFT performed within the time interval 100 s $\leqslant t \leqslant$ 140 s after the pulse shows two distinct peaks on the $n = 2$ line occurring at $f \approx 0.4$ Hz and $f \approx 0.2$ Hz (see figure 7). The higher frequency of $f \approx 0.4$ Hz is clearly detectable in the spatio-temporal velocity plot (figure 6*a*). That this dominant $(\gamma_1, 2)$ mode is superposed with a second inertial wave mode is evident

https://doi.org/10.1017/jfm.2014.371 Published online by Cambridge University Press

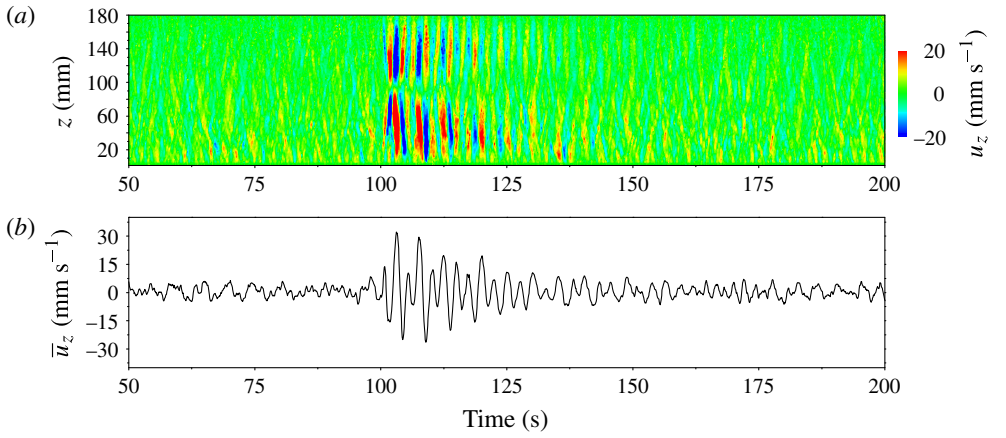


FIGURE 6. Free inertial wave along the axis of the rotating liquid metal column excited by an azimuthally directed pulse; $B_R = 1.3$ mT. Pulse: $t = 100$ s; $\Delta t_p = 0.2$ s; $B_R = 6.3$ mT. (*a*) Axial velocity at $r/R_0 = 0$; (*b*) mean axial velocity averaged along the lower half of the cylinder, $0 \leqslant z \leqslant H_0/2$.

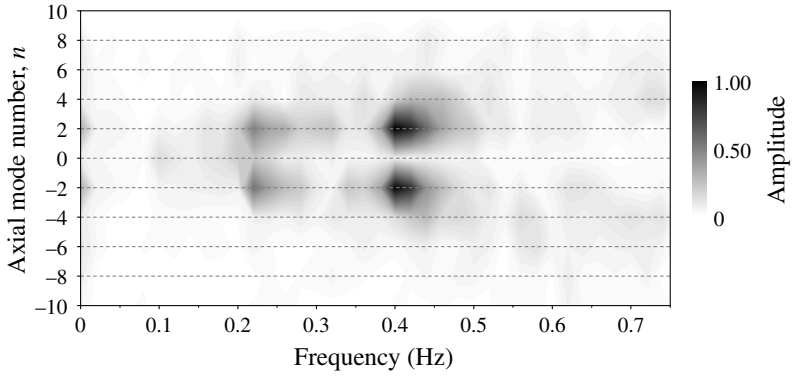


FIGURE 7. The 2D-FFT of the spatio-temporal flow structure excited by the RMF pulse (corresponding to the measurement shown in figure 6*a*). FFT time interval: 100 s $\leqslant t \leqslant$ 140 s.

in figure 6(*b*), which reveals a modulation in the amplitude of the mean axial velocity. This axial velocity was averaged over only the lower half of the vessel axis, as the inertial wave mode is antisymmetric about the midpoint of the axis. Comparing the frequencies to the linear theory (see § 6) shows that this second inertial wave has the same axial wavenumber ($n = 2$), but a higher radial wavenumber (γ_2, 2). That is, the (γ_1, 2) cell in the lower half of the vessel (where the mean axial velocity was averaged) is alternatingly co- or counter-rotating with the second inertial mode every second cycle, leading to the observed modulation of the velocity amplitude.

The excitation of the (γ_i, 2) wave modes becomes plausible by considering the vertical distribution of the RMF-induced Lorentz force (Gorbachev *et al.* 1974). The azimuthal acceleration on the liquid metal is higher at the half-height of the vessel as compared to the acceleration near the top and bottom walls. The consequence is an axial gradient of the azimuthal velocity ($\partial u_\phi / \partial z$). This leads to an axial imbalance of

https://doi.org/10.1017/jfm.2014.371 Published online by Cambridge University Press

the centrifugal force and, in turn, an axial pressure gradient. This pressure gradient drives (γ_i, 2) inertial waves, which have a symmetry plane at the half-height of the vessel. The same mechanism drives the inertial waves during the spin-up phase of an RMF-driven liquid metal flow (see Nikrityuk *et al.* 2005; Räbiger *et al.* 2010).

6. Comparison to the linear theory

In the previous sections, we used the linear theory to identify the inertial wave modes. Because of the deviation from solid-body rotation of the flow under consideration, we have to confirm that the application of the linear theory is justified in our case. Therefore, we present in this section a detailed comparison between the characteristic frequencies of the inertial modes, as detected in the experiments after a single RMF or TMF pulse, and the corresponding predictions from the linear theory. For this purpose, we performed a further series of measurements using three cylinders with different aspect ratios of $A = 1$, 2 and 3. This set of experiments was carried out in the same way as the experiments described in § 5. The liquid metal was driven by a continuous RMF for a sufficiently long time in order to ensure a quasi-stationary rotating motion inside the cylinder. The rotating liquid metal was then exposed to a strong, but short-lived, magnetic field pulse in order to trigger a free inertial wave. This procedure was repeated for all three aspect ratios, for different rotation rates, and for axial and azimuthal directed magnetic field pulses by means of a TMF or RMF, respectively. The frequencies of the inertial waves were determined by an FFT of the measured axial velocity and compared with the linear theory of inertial waves, derived first by Kelvin (1880) and later by Bjerknes & Solberg (1929), for inviscid inertial waves in a straight circular cylinder. While a very detailed derivation of this problem can be found in Greenspan (1968), here we refer only to the final solution of this linear theory, which can be compared to our experiments. The dimensionless frequency ξ of a given (γ_i, n, m) inertial wave can be calculated from the following equation:

$$\xi = 2\left[1 + \left(\frac{\gamma_i}{n\pi}\right)^2 \left(\frac{H_0}{R_0}\right)^2\right]^{-1/2}. \tag{6.1}$$

The wavenumbers in the axial (n) and azimuthal (m) directions are both integers. The radial wavenumber γ_i, which is not an integer, follows from

$$\gamma_i \, \mathrm{J}'_m(\gamma_i) + m\left[1 + \left(\frac{\gamma_i}{n\pi}\right)^2 \left(\frac{H_0}{R_0}\right)^2\right]^{1/2} \mathrm{J}_m(\gamma_i) = 0. \tag{6.2}$$

In the case of an axisymmetric inertial wave ($m = 0$), (6.2) reduces to

$$\mathrm{J}'_0(\gamma_i) = 0. \tag{6.3}$$

According to $\mathrm{J}'_0(\gamma_i) = -\mathrm{J}_1(\gamma_i)$, the radial wavenumbers for all $m = 0$ inertial waves are the roots of the first-order Bessel function $\mathrm{J}_1(\gamma_i)$, namely $\gamma_1 = 3.832$, $\gamma_2 = 7.016$ and $\gamma_3 = 10.174$, etc. The conversion of (6.1) into a dimensional form gives

$$f_{\gamma_i,n} = \frac{\Omega}{\pi}\left[1 + \left(\frac{\gamma_i}{n\pi}\right)^2 \left(\frac{H_0}{R_0}\right)^2\right]^{-1/2}. \tag{6.4}$$

https://doi.org/10.1017/jfm.2014.371 Published online by Cambridge University Press

Equation (6.4) is the solution of the inertial wave problem for an inviscid fluid enclosed by a rotating, circular cylinder. The boundary condition requires the no-slip condition at the inner wall of the cylinder. This means that the fluid at steady state rotates with the same angular velocity as the cylinder. The fluid is therefore at rest in the rotating frame of reference. Fultz (1959) performed experiments as proof of inertial waves in a rotating cylinder. For that purpose, a small plate inside the rotating cylinder was vibrated at controllable frequencies in order to force various axisymmetric ($m = 0$) inertial wave modes. Since the fluid inside the cylinder was in almost quasi-solid-body rotation, the remarkably close agreement between the frequency measurements and predictions from the linear theory was to be expected.

Equation (6.4) shows a linear dependence of the frequencies of the inertial wave modes on the angular velocity (Ω). This parameter was determined by measurements of the azimuthal velocity of the liquid metal, where a UDV sensor was placed at the mid-height of the respective cylindrical vessel. The ultrasonic beam is directed horizontally along a chord at a radial distance of $r_s = 5$ mm from the vessel axis (see figure 1). This configuration allows for the reconstruction of the azimuthal velocity from the measured velocity (u_m) according to

$$u_m = u_\phi \sin(\alpha) + u_r \cos(\alpha), \tag{6.5}$$

where u_ϕ is the azimuthal velocity and u_r is the radial velocity component. The angle α is defined in figure 1. In the case of an axisymmetric flow, the azimuthal velocity can be calculated as

$$\Omega(r) = \frac{u_\phi}{r} = \frac{1}{2r_s}(u_m(+\alpha) + u_m(-\alpha)). \tag{6.6}$$

The reconstruction of the angular velocity is valid in a radial range of $r_s \leqslant r \leqslant 0.95R_0$. The accuracy of the measured data in the region close to the vessel walls is limited by the interaction of the ultrasonic beam with the curved sidewall. Figure 8 displays the result of this angular velocity reconstruction for the different aspect ratios $A = 1$, 2 and 3. The values of B_R in this figure were varied in order to get approximately the same rotation rate in the different aspect ratios. The profiles demonstrate the non-uniformity of the liquid metal rotation inside the cylinder. Instead, an almost linear decrease of the angular velocity from the vessel axis to the sidewall of the vessel can be observed. Note that the velocity drop in the sidewall boundary layer cannot be resolved. For a comparison between our measured frequencies and the predictions from the linear theory, we need to calculate a volume-averaged rotation rate ($\bar{\Omega}$). Therefore, we approximated the measured angular velocity distribution by a linear fit and integrated this fitting function along the vessel radius as

$$\bar{\Omega} = \frac{2}{R_0^2}\int_{r=0}^{R_0} r\Omega_{fit}(r)\,\mathrm{d}r. \tag{6.7}$$

This volume-averaged angular velocity was inserted into (6.4) to calculate the inertial wave frequencies. The results are shown in figure 9. The lines in figure 9 represent the theoretical values of the (γ_1, 1) inertial wave and the (γ_1, 2) inertial wave, which are the main modes triggered in the experiments by the TMF and RMF pulse, respectively. The corresponding measurements are displayed by the symbols. The influence of the boundary layers at the top and bottom of the vessel leads to the real volume-averaged angular velocity being lower than the angular velocity calculated using (6.7), which

https://doi.org/10.1017/jfm.2014.371 Published online by Cambridge University Press

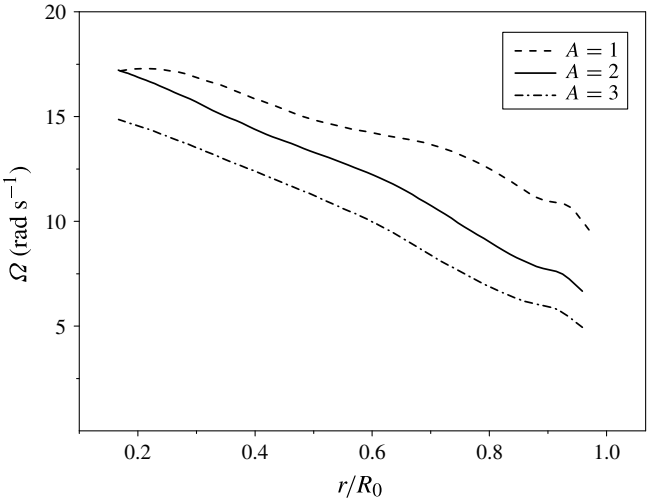


FIGURE 8. Radial profiles of the liquid metal angular velocity at $z = H_0/2$ for the different aspect ratios $A = 1$ (measured at $B_R = 3.7$ mT), $A = 2$ (measured at $B_R = 2$ mT) and $A = 3$ (measured at $B_R = 1.5$ mT).

in turn leads to a frequency shift between the theoretical curves and the experimental data. Our simplified analysis does not take into account the non-uniform distribution of the angular velocity along the cylinder height. There is an axial gradient of the swirling flow caused by the horizontal boundary layers retarding the rotating fluid in their vicinity. The relative influence of these boundary layers becomes smaller at higher aspect ratio, and it thus seems plausible that a better agreement between linear theory and our experiment was found here. In general, it can be concluded that the measured frequencies are in reasonable agreement with the predictions from the linear theory. Deviations issue from the imprecise determination of the angular velocity. Of course, the presented comparison is only a rough estimate, and it would be possible to get a better agreement by some adaptations of the linear theory to our special case, but this is beyond the scope of this study.

For a further comparison of the linear theory and our experimental data, we have to reconsider the measurement of the spontaneously excited inertial wave and the corresponding 2D-FFT shown in figure 3. The strongest peak in this 2D-FFT is at $f \approx 0.19$ Hz and corresponds to the $(\gamma_1, 1)$ inertial wave. Knowing this, one can calculate the theoretical angular velocity of the fluid with (6.4) to be $\Omega = 4.4$ rad s^{-1}, which allows us to calculate the expected frequencies of the different wave modes as shown in table 2. A reconsideration of figure 3 reveals that there is reasonable evidence for the modes $(\gamma_2, 1)$, $(\gamma_1, 1)$, $(\gamma_2, 3)$, $(\gamma_1, 2)$, $(\gamma_2, 4)$, $(\gamma_1, 3)$ and $(\gamma_1, 4)$. This comparison also underlines that the frequency of inertial waves occurring even in a rather complex flow structures can be predicted analytically quite reasonably. The Ekman number for the considered flow is about $E = \nu/(\Omega R_0^2) \sim 10^{-4}$. Thus, the good agreement is consistent with the finding of Hollerbach & Kerswell (1995) that the viscous frequency shift for such small Ekman numbers is below 1 %.

7. Forced inertial waves generated by a modulated magnetic field

In this section, we present experiments where a pulsating RMF was used to force particular inertial wave modes in the liquid metal column. The experimental

https://doi.org/10.1017/jfm.2014.371 Published online by Cambridge University Press

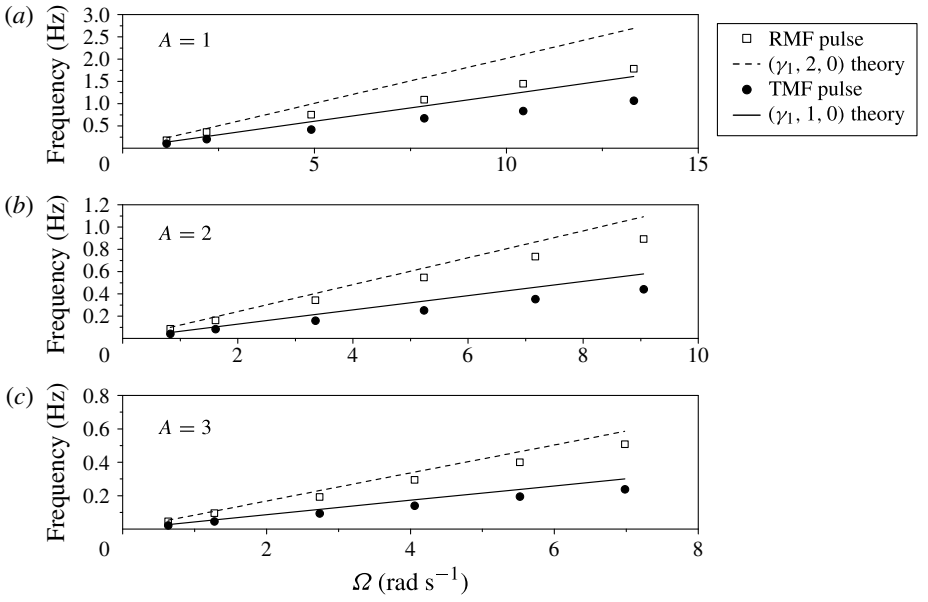


FIGURE 9. Comparison of the measured inertial wave frequencies (symbols) to the predictions of the linear theory (lines) for three different aspect ratios A.

Inviscid	$n=1$	$n=2$	$n=3$	$n=4$	$n=5$	$n=6$	$n=7$	$n=8$
γ_1	0.19	0.37	0.53	0.67	0.79	0.89	0.97	1.03
γ_2	0.10	0.21	0.31	0.40	0.49	0.57	0.65	0.72
γ_3	0.07	0.14	0.21	0.28	0.35	0.41	0.47	0.53

TABLE 2. Expected frequencies at $\Omega = 4.4$ rad s^{-1} in aspect ratio $A = 3$ according to figure 3.

set-up remains unchanged, but the type of electromagnetic forcing provided now is a sequence of equidistant rectangular RMF pulses, as shown in figure 10. Such a pulsating RMF implies periodic changes of the driving force. The fluid rotates because of inertia and the constant direction of the angular acceleration. The different inertial wave modes can be excited by a variation of the frequency of the RMF pulses ($f_p = 1/T_p$), which is the main parameter in these experiments. Measurements were conducted where the pulse frequency was varied in very fine steps from $f_p = 0.04$ Hz to 0.5 Hz while the amplitude of the RMF pulses was kept constant at $B_R = 1$ mT. Several inertial wave modes were identified in this pulse frequency range. A given inertial mode appears at its largest possible intensity when the pulse frequency coincides with the natural frequency of the respective mode. This kind of resonance can be detected by drawing the time-averaged root-mean-square velocity as a function of the pulse frequency (figure 11). This value was calculated as

$$\bar{u}_{z,rms} = \frac{1}{t_N} \sum_{i=1}^{t_N} u_{z,rms}, \tag{7.1}$$

https://doi.org/10.1017/jfm.2014.371 Published online by Cambridge University Press

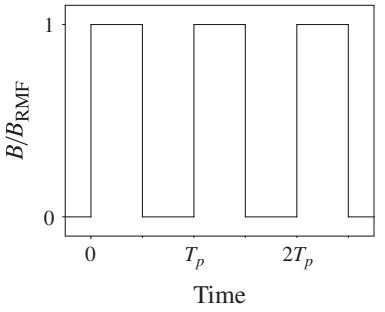


FIGURE 10. Modulation scheme of the applied pulsating RMF.

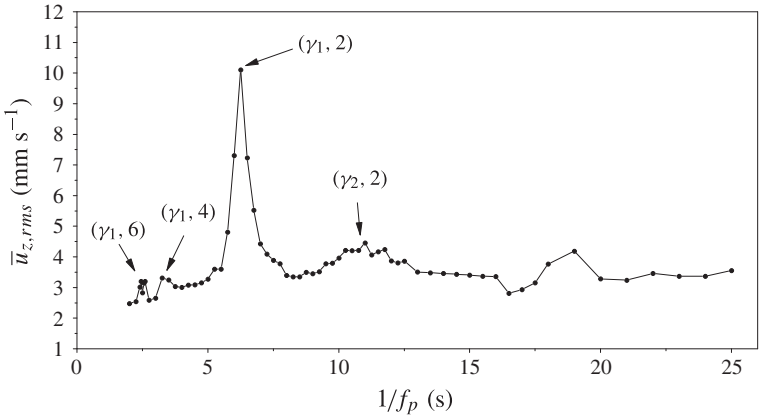


FIGURE 11. Time-averaged root-mean-square velocity at different pulse frequencies; $r/R_0 = 0$; $A = 3$; $B_R = 1$ mT.

where t_N represents the number of measured time steps. We focus on the particular maxima, on the left ($1/f_p \leqslant 10$ s) in figure 11, that can be related to respective resonance frequencies (f_r) of specific inertial wave modes. In contrast, the broad maxima and minima above $1/f_p \geqslant 10$ s are a result of superpositions of multiple inertial wave modes with resonance frequencies that are very close to each other. To give an example, the resonance frequency of the $(\gamma_2, 2)$ inertial wave is $1/f_r \approx 11$ s, which is very close to the half-resonance frequency of the $(\gamma_1, 2)$ inertial wave at $2/f_r \approx 12.5$ s. A further resonance peak of the $(\gamma_1, 4)$ inertial wave occurs at a third of their resonance frequency ($3/f_r \approx 10$ s). Consequently, all these modes interact with each other. This range of forcing frequencies, where the mixed modes occur, will only briefly be discussed at the end of this section.

Figure 11 reveals the $(\gamma_1, 2)$ inertial wave mode as the dominating inertial mode whose intensity at the resonance significantly exceeds all other modes. A corresponding measurement at a pulse frequency of $f_p = 0.16$ Hz ($1/f_p \approx 6.25$ s) can be seen in figure 12. The spatial structure of the $(\gamma_1, 2)$ wave resembles the structure of the Ekman-driven recirculation tori of the secondary flow described in § 2. This conformance, as well as the fact that the spatial structure of this wave mode is supported by the RMF-induced force distribution, are the reasons for the prominent role of this mode, which can be designated as the fundamental mode in the configuration of an RMF-driven flow in a closed cylinder.

https://doi.org/10.1017/jfm.2014.371 Published online by Cambridge University Press

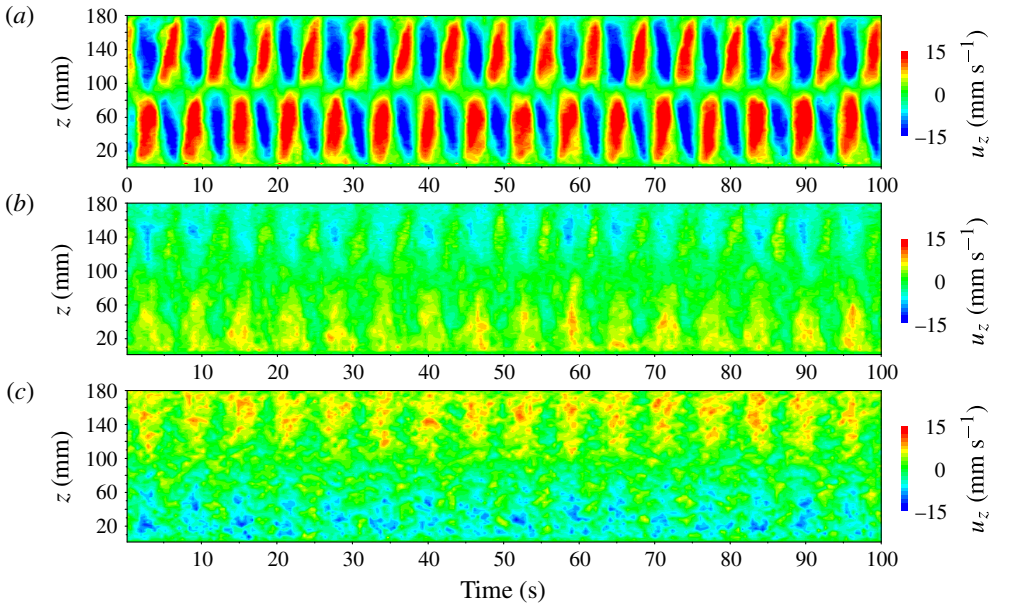


FIGURE 12. The $(\gamma_1, 2)$ inertial wave mode excited by a pulsating RMF; $B_R = 1$ mT; $f_p = 0.16$ Hz. Axial velocity at (*a*) $r/R_0 = 0$, (*b*) $r/R_0 = 0.45$ and (*c*) $r/R_0 = 0.9$.

The flow pattern associated with the $(\gamma_1, 2)$ mode (see figure 12*a*) shows periodic flow reversals along the rotational axis of the vessel, with positive and negative velocity amplitudes having almost the same intensity. While the flow in the centre of the vessel is clearly dominated by the inertial wave, a different flow pattern occurs at the other radial positions (figure 12*b*,*c*). Outside the inner core of the vessel, the flow pattern is characterized by a superposition of the inertial wave with the two counter-rotating recirculation tori from the secondary flow. The speckled structure of the velocity plot near the sidewall (figure 12*c*) indicates the presence of turbulent flow with smaller vortex structures. A comparison of the phasing at the three radial positions shows that the vertical velocity at sensors 1 and 2 are in phase, while a change of sign can be observed in the velocity recorded at sensor 3. This provides an indication regarding the spatial manifestation of the $(\gamma_1, 2)$ mode. The highest flow intensities appear at the cylinder axis. The inner leg of the toroidal vortex spans over a wide area around the cylinder axis, whereas the return flow is restricted to the region near the sidewalls.

A comparison of the velocity signal recorded at the three outer sensors 3, 4 and 5 (figure 13) shows that the inertial wave is in phase at different azimuthal positions. Thus, the considered inertial wave is in fact axisymmetric ($m = 0$), as expected.

The flow measurements presented in the previous section have shown that two or more different inertial wave modes may appear simultaneously after a short single RMF pulse and in the case of the spontaneously excited inertial wave. The 2D-FFT in figure 14 shows that multiple inertial wave modes can also be observed simultaneously in the case of periodic forcing at the fundamental resonance frequency. In addition to the dominating fundamental inertial mode $(\gamma_1, 2)$, we can clearly identify further harmonic inertial wave modes in figure 14. In particular, there is a $(\gamma_1, 4)$ inertial wave appearing at double the pulsating frequency, a $(\gamma_1, 6)$ inertial wave with frequency

https://doi.org/10.1017/jfm.2014.371 Published online by Cambridge University Press

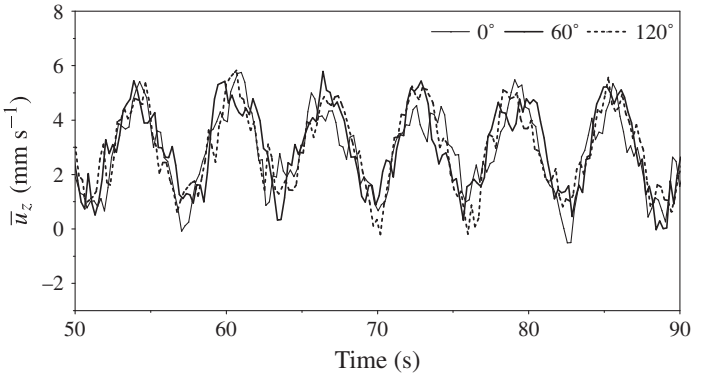


FIGURE 13. Axial symmetry of the inertial wave: mean vertical velocity recorded at three different azimuthal positions and averaged along the upper half of the cylinder, $H_0/2 \leqslant z \leqslant H_0$; $B_R = 1$ mT; $f_p = 0.16$ Hz; $r/R_0 = 0.9$.

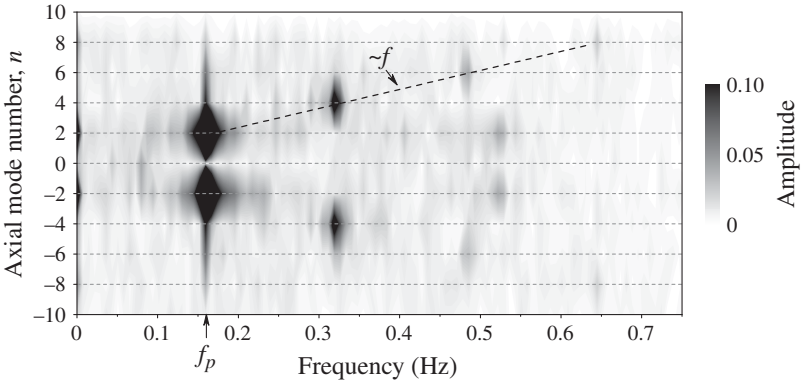


FIGURE 14. The 2D-FFT of the spatio-temporal flow structure recorded at the resonant period of the $(\gamma_1, 2)$ wave mode (corresponds to the measurement shown in figure 12*a*); $B_R = 1$ mT; $f_p = 0.16$ Hz; $r/R_0 = 0$.

three times the pulsating frequency and a very weak $(\gamma_1, 8)$ inertial wave having four times higher frequency. From (6.4) we can derive that the specific frequencies of the higher modes $(\gamma_1, 4)$, $(\gamma_1, 6)$ and $(\gamma_1, 8)$ are not integer multiples of the $(\gamma_1, 2)$ frequency, which is in contrast to the fact that the different modes in figure 14 can be fitted by the dashed straight line. In other words, the frequencies of the higher modes do not match the expected frequencies. Thus, the coexistence of the different inertial wave modes in this measurement is only possible if the higher modes are flexible to adapt their frequency to integer multiples of the excitation frequency.

These measurements furthermore confirm the general rule: the higher the wavenumber, the lower the amplitude of the inertial wave. This observation is plausible, because smaller waves convey less energy and are more affected by viscous dissipation.

Figure 12(*a*) also reveals slightly 'inclined' or 'skewed' flow structures. The red structures are inclined to the right, whereas the blue structures are slightly inclined to

https://doi.org/10.1017/jfm.2014.371 Published online by Cambridge University Press

the left, which suggests that the inertial wave could be a travelling wave. The reason for this inclination is presumably the previously discussed superposition of different harmonic wave modes. In principle, the flow pattern shown in figure 12(*a*) can be generated by a superposition of different travelling wave modes, since every standing wave can be decomposed into two propagating waves with a phase shift of 180°. This becomes visible in our FFT plots. However, the forward and reflected waves in the FFT (equal to positive and negative quadrant in the FFT plots) have equal frequencies and equal amplitudes, so that we interpret it as a standing wave. A similar inclination of flow structures in the spatio-temporal velocity plots was observed by Eckert *et al.* (2007), who studied the flow during a single RMF pulse. This situation is equivalent to an interrupted RMF-driven spin-up, where the flow resulting from the spin-up interferes with the starting spin-down process. Such a scenario gives reason to expect a superposition of different wave modes.

We now consider the phenomenon called 'resonant collapse' of inertial waves, which was observed and annotated in earlier experimental studies. Manasseh (1992) investigated the flow in a rotating cylinder subjected to precessional forcing. The completely filled cylinder was turned around its symmetry axis until the fluid reached a solid-body rotation. The cylinder was then subjected to forced precession at various excitation frequencies, nutation angles and Ekman numbers. This method of forcing can excite selected inertial modes within the fluid. He reported that forcing close to the resonance of the fundamental mode generates an inertial wave that collapses suddenly into small-scale structures shortly after the onset of the precessional forcing. Kobine (1995) performed some experiments similar to those performed by Manasseh (1992). The difference between these two experimental studies is the frame of reference in which the flow measurements were made. Manasseh used a stationary camera for his flow visualization, while Kobine applied a laser Doppler velocimetry system in co-rotation with the cylinder and thus measured the dynamics in a rotating frame of reference. Consequently, he observed a continuous evolution from a regular to an irregular behaviour of the inertial waves instead of an abrupt 'resonant collapse' as observed by Manasseh three years before.

Kobine (1995) figured out that, even in the fully developed nonlinear regime following the 'resonant collapse', the dynamics of the flow are much simpler than suggested before by flow visualization experiments. Furthermore, he analysed the power spectra of the velocity signals for a long period beyond the 'resonant collapse' in order to understand the features of the fully developed nonlinear regime. He detected a strong peak in the power spectra at $f = f_p$ and a small peak at $f = 2f_p$, and, in the case of strong forcing (large nutation angles), he found frequencies in his velocity signal at $f = f_p/2$. It is reasonable to conclude that the 'resonant collapse' of inertial waves might be caused by nonlinear interactions between different wave modes. Such an assumption is supported by our experiments, as there is no chaotic flow response observed at the resonant pulse frequency of the fundamental mode. However, one has to keep in mind the crucial difference between the precessional moving cylinder and our set-up. We excite axisymmetric inertial wave modes ($m = 0$), whereas a precessing cylinder creates only non-axisymmetric inertial waves ($m \neq 0$). Nevertheless, in agreement with the measurements made by Kobine (1995), the power spectra of our measurements (figure 14) reveal the existence of harmonic inertial waves. In addition to the $2f_p$ harmonic, we detected higher modes at $3f_p$ and $4f_p$. Our experiments do not show any evidence for the existence of a phenomenon like 'resonant collapse'. The flow response at resonance shows a very regular flow structure that results from the superposition of different inertial wave modes.

https://doi.org/10.1017/jfm.2014.371 Published online by Cambridge University Press

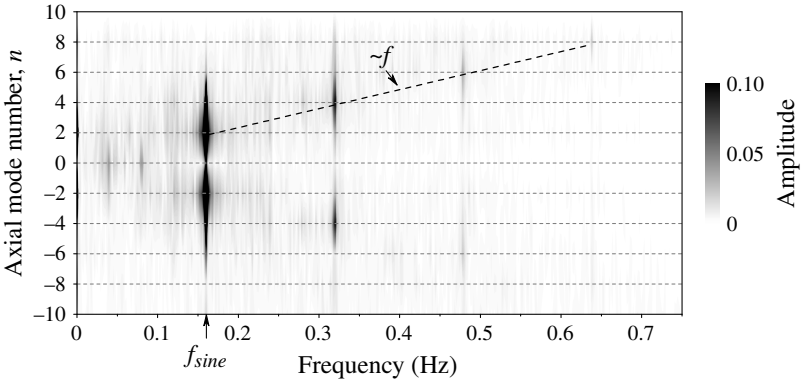


FIGURE 15. The 2D-FFT of the spatio-temporal flow structure forced with a sinusoidal modulated RMF $(\gamma_1, 2)$ inertial wave; $B_{R,sine} = 1.1$ mT; $f_p = 0.16$ Hz; $r/R_0 = 0$.

To ensure that the observation of these harmonic inertial wave modes is not an artefact due to the specific forcing with rectangular RMF pulses, we repeated the previously presented measurements with a different modulation of the RMF pulses. Instead of rectangular pulses, we now used a sinusoidal modulated RMF, where the frequency of the sine wave was identical to the pulse frequency of the previously used rectangular RMF pulses ($f_{sine} = f_p = 0.16$ Hz). To compensate the difference in the energy input that arises from the application of a sinusoidal driving force, the amplitude of the sine function was increased by a factor of $\sqrt{4/3}$ to a value of $B_{R,sine} = 1.1$ mT. The 2D-FFT of this sinusoidal forced inertial wave at the fundamental resonance is depicted in figure 15. The flow structure obtained by sinusoidal forcing is almost identical with the flow pattern generated by the rectangular pulses. Higher harmonic inertial wave modes occur just as in figure 14. This result gives evidence that the occurrence of higher inertial wave modes is a common feature not related to the particular type of forcing.

The higher axial wave modes that appeared in the case of the fundamental resonance in addition to the fundamental $(\gamma_1, 2)$ inertial wave can be generated directly if the pulse frequency is adapted to their specific resonance frequency. Figures 16 and 18 display measurements at three radial positions, where the frequency of the RMF pulses fits the resonance points of the $(\gamma_1, 4)$ and the $(\gamma_1, 6)$ inertial wave, respectively. These higher axial wave modes are only visible in the central region of the vessel. The flow field in the outer part is dominated by the recirculation tori from the secondary flow disturbed by series of TG vortices (Vogt *et al.* 2012). Figures 17 and 19 show the corresponding 2D-FFT results. In contrast to the fundamental $(\gamma_1, 2)$ inertial wave, the 2D-FFT of these higher inertial wave modes shows only one peak at their specific frequency and further weak peaks of the $(\gamma_1, 2)$ and $(\gamma_1, 1)$ wave modes. This means that there are no higher harmonics, which might be explained as follows.

The maximum flow intensity is related to the fundamental resonance $(\gamma_1, 2)$ and can be achieved by forcing with RMF pulses at a frequency of $f_p = 0.16$ Hz. The energy manifesting in the $(\gamma_1, 4)$ and the $(\gamma_1, 6)$ inertial wave modes remains significantly lower. At the same time, the turbulence intensity increases, as can be observed in figure 16(*b*,*c*) and figure 18(*b*,*c*). However, we can assume an equal input of energy, averaged over time, transferred from the pulsating RMF to the flow for all pulse

https://doi.org/10.1017/jfm.2014.371 Published online by Cambridge University Press

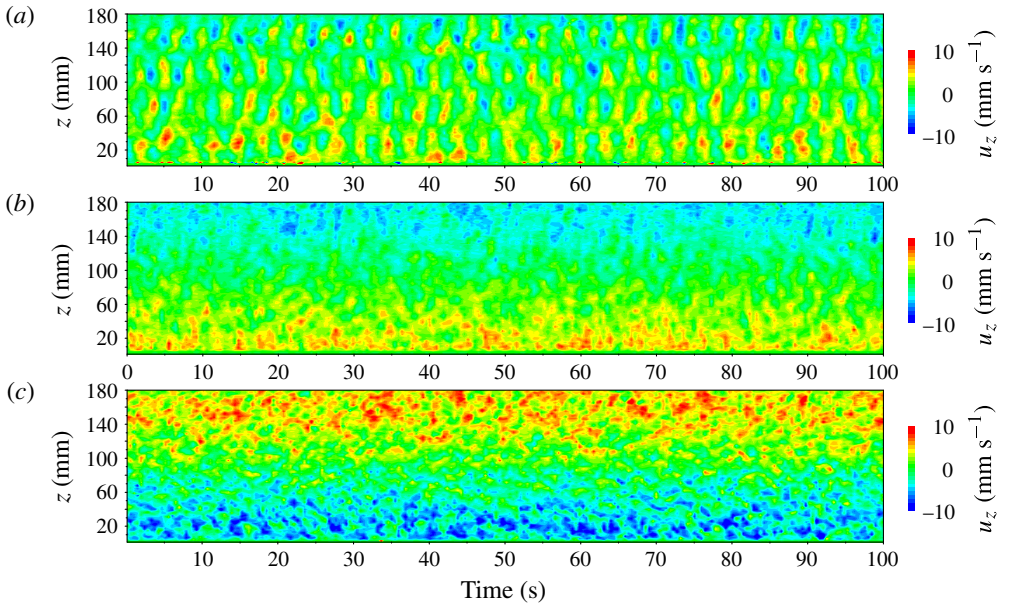


FIGURE 16. The $(\gamma_1, 4)$ inertial wave mode excited by a pulsating RMF; $B_R = 1$ mT; $f_p = 0.31$ Hz. Axial velocity at (*a*) $r/R_0 = 0$, (*b*) $r/R_0 = 0.45$ and (*c*) $r/R_0 = 0.9$.

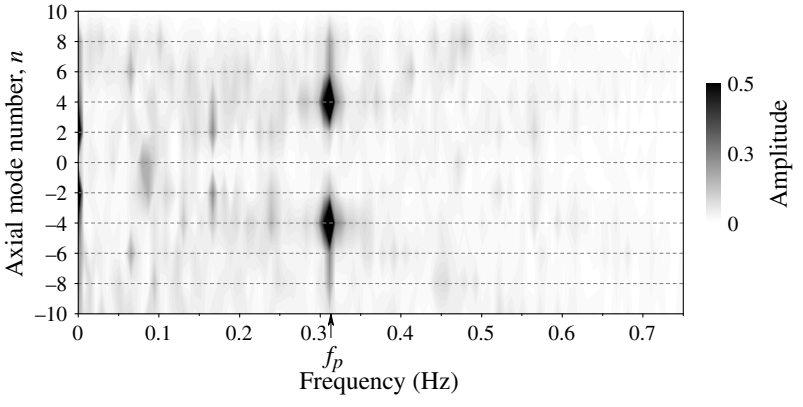


FIGURE 17. The 2D-FFT of the spatio-temporal flow structure recorded at the resonant period of the $(\gamma_1, 4)$ inertial wave (corresponds to the measurement shown in figure 16*a*); $B_R = 1$ mT; $f_p = 0.31$ Hz; $r/R_0 = 0$.

frequencies applied. This means that a large amount of the energy coming from the pulsating RMF is dissipated into turbulent structures if the pulse frequency is different from the fundamental resonance. At the end, the higher harmonics do not have a chance to survive in a turbulent flow when the wavelength of the higher modes approaches the same order of magnitude as the characteristic size of the turbulent structures.

The previous discussion of the results focused on the range of frequencies above the fundamental resonance mode. Two effects can be observed for frequencies lower

https://doi.org/10.1017/jfm.2014.371 Published online by Cambridge University Press

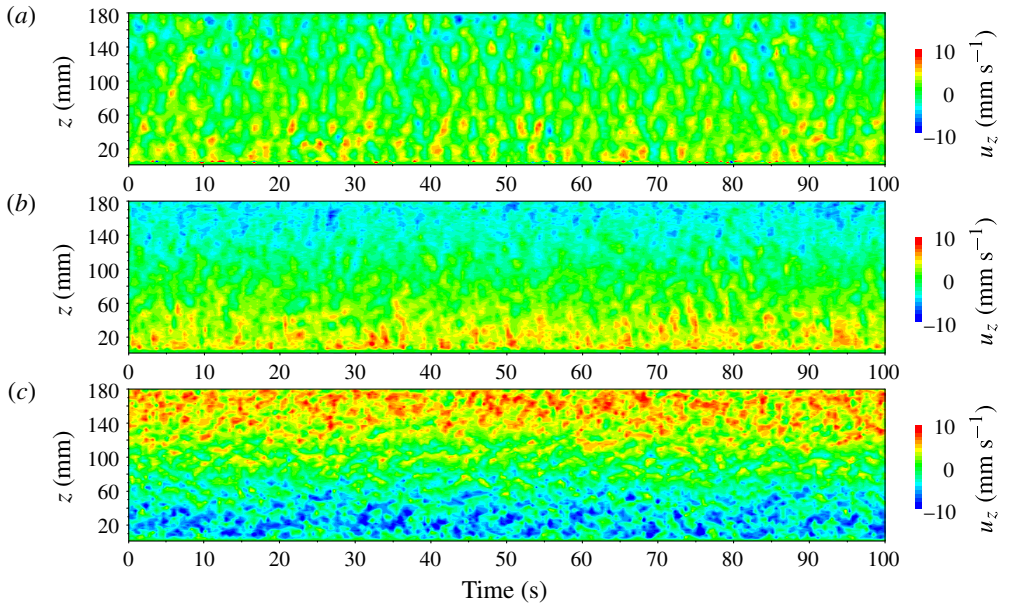


FIGURE 18. The $(\gamma_1, 6)$ inertial wave mode excited by a pulsating RMF; $B_R = 1$ mT; $f_p = 0.4$ Hz. Axial velocity at (*a*) $r/R_0 = 0$, (*b*) $r/R_0 = 0.45$ and (*c*) $r/R_0 = 0.9$.

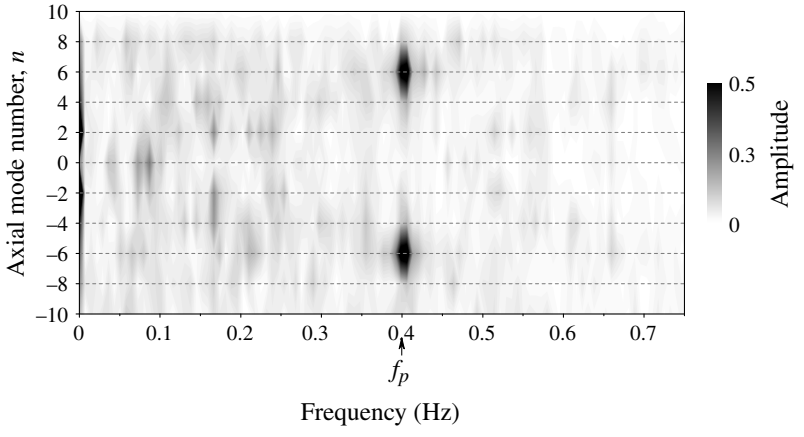


FIGURE 19. The 2D-FFT of the spatio-temporal flow structure recorded at the resonant period of the $(\gamma_1, 6)$ inertial wave (corresponds to the measurement shown in figure 18*a*); $B_R = 1$ mT; $f_p = 0.4$ Hz; $r/R_0 = 0$.

than the fundamental resonance. The first is an increase of the radial mode number, as shown in a previous experimental study (Räbiger *et al.* 2012), where an ultrasound array was used to measure the flow field over the entire vessel radius. The second effect is an excitation of $(\gamma_i, 2)$ inertial wave modes at multiples of their resonant period, a phenomenon described in § 5.2 (excitation by an azimuthally directed pulse). These two effects occur very close to each other, which is why it is difficult to trigger one specific inertial wave mode at pulse frequencies below the fundamental

https://doi.org/10.1017/jfm.2014.371 Published online by Cambridge University Press

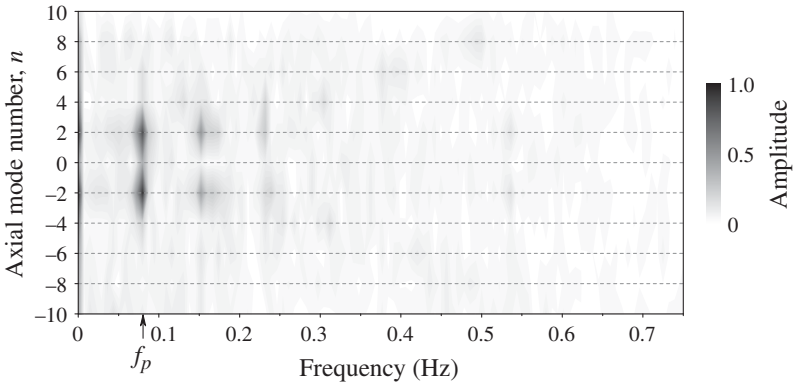


FIGURE 20. Simultaneous appearance of different radial inertial wave modes. The 2D-FFT of the spatio-temporal flow structure recorded at $f_p = 0.077$ Hz; $B_R = 1$ mT; $r/R_0 = 0$.

resonance. Instead, we observed several inertial wave modes simultaneously, as shown in figure 20. The strongest peak in this figure can be found at the pulse frequency of 0.07 Hz. It matches the frequency of the higher radial inertial wave mode $(\gamma_2, 2)$. The second maximum can be found at $f = 2f_p = 0.15$ Hz, which is close to the resonant period of the $(\gamma_1, 2)$ inertial wave mode at 0.16 Hz. A similar superposition of inertial waves with different radial mode numbers was observed and already discussed in § 5.2.

8. Conclusions

In this work, the dynamics of free and forced inertial waves were studied inside cylinders of different aspect ratios $A = H_0/2R_0$. Our experimental study demonstrates that inertial waves can be investigated in depth using a contactless forcing of a liquid metal flow by means of electromagnetic fields. The highly accurate magnetic induction system MULTIMAG at HZDR generated an RMF that induced a swirling motion inside the liquid metal. The application of short electromagnetic field pulses or time-modulated electromagnetic fields provides a high flexibility with respect to the excitation of various inertial wave modes on the background of this RMF-driven rotating flow. The flow pattern and the characteristics of the inertial waves were detected through UDV. The time-modulated AC fields turned out to be an efficient method for triggering inertial waves.

A prominent feature of our experimental configuration is the interaction between the inertial modes and the secondary flow arising from the Ekman pumping. This became obvious in a first set of experiments, where we observed the formation of a $(\gamma_1, 1)$ inertial wave mode even without any external triggering by deliberate disturbances of the rotating flow field. This spontaneous excitation can be explained by the existence of TG vortices at the sidewall of the vessel. These TG vortices are conveyed by the secondary flow towards the top and bottom of the vessel, where they dissipate in the Bödewadt layer. This vortex dissipation in the Bödewadt layer perturbs the Ekman pumping, exciting an inertial wave. This mechanism is not the same as that found in the numerical study by Sauret *et al.* (2005), who reported the emission of inertial waves from the turbulent sidewall layers and the corner of a librating cylinder. The inertial waves observed in the present work, as well as in recent studies (Zhang *et al.* 2011; Vogt *et al.* 2012), emanate from the Bödewadt layers into the

https://doi.org/10.1017/jfm.2014.371 Published online by Cambridge University Press

bulk zone. Moreover, the evolution of the amplitudes of the spontaneously triggered $(\gamma_1, 1)$ inertial wave showed an unexpected behaviour. While an exponential decay of the inertial wave amplitude would seem to be natural, the experiments show a continuity of the $(\gamma_1, 1)$ inertial wave over many periods at a constant amplitude. This interesting behaviour is probably caused by an interaction of the inertial wave with the Bödewadt layer at the top and bottom walls of the vessel. This interplay enables a periodic transfer of energy from the Ekman flow to the inertial wave. More research on this interesting issue is beyond the scope of this paper, but worth addressing in a forthcoming paper.

A second set of experiments investigated the behaviour of free waves generated by a strong perturbation of the flow. For that purpose, the somewhat arbitrary inertial wave excitation by TG vortices was replaced by a well-defined and reproducible excitation scheme, based on a steady rotating flow driven by a constant RMF inside the liquid metal. After a certain time, this flow was disturbed by a singular and short magnetic field pulse in either the axial or azimuthal direction. This impulsive perturbation of the flow triggers a free inertial wave inside the liquid metal. For an azimuthally directed electromagnetic pulse, the generated inertial wave appears as a $(\gamma_1, 2)$ mode with a superimposed $(\gamma_2, 2)$ mode. For an axially directed pulse, we found a $(\gamma_1, 1)$ inertial wave. The evolution of the amplitudes of this free $(\gamma_1, 1)$ inertial wave showed the same self-preserving behaviour as the inertial wave triggered by internal turbulence. In contrast, other inertial wave amplitudes excited by the azimuthally directed pulse show the expected exponential decay owing to the fluid viscosity. Thus, the self-preserving behaviour of inertial waves seems to be restricted to the $(\gamma_1, 1)$ mode. This finding is consistent with the mechanism, described above, being responsible for an energy transfer from the Bödewadt layer to the inertial wave.

The frequencies of $(\gamma_1, 1)$ and $(\gamma_1, 2)$ inertial waves found at different aspect ratios of the cylinders and different rotation rates of the fluid were compared with the predictions of the linear inviscid theory. Although the flow field in our experiment shows developed boundary layers, turbulence and a non-uniform angular velocity distribution, the agreement between the measured frequencies and the linear theory is quite reasonable. The retarding influence of the Bödewadt layer at the top and bottom walls of the vessel on the bulk flow means that higher cylinder aspect ratios have better agreement.

The last part of this work focused on a permanent forcing of inertial waves. These forced inertial waves were generated by equidistant rectangular RMF pulses, where the pulse repetition frequency was the main parameter. The variation of this pulse frequency enabled the selective excitation of several inertial wave modes, separately or simultaneously. The increase of the pulse frequency yields an increase of the axial mode number of the excited inertial waves. In the case of low pulse frequencies, inertial waves with higher radial mode numbers are generated. An exceptional flow structure was observed when the pulse frequency matches the fundamental resonance of the $(\gamma_1, 2)$ mode. In this case, very high amplitudes and the occurrence of several higher harmonic inertial wave modes can be observed. Our experiments do not show any evidence for the existence of a phenomenon called 'resonant collapse'. Instead, forcing at the fundamental resonance yields a well-structured flow that can be clearly decomposed into different harmonic inertial wave modes. The reason for this might be the axial symmetry of our flow field ($m = 0$). Harmonic inertial wave modes at the fundamental resonance are not induced exclusively by rectangular RMF pulses. A measurement at the fundamental resonance, where the RMF was modulated sinusoidal, revealed the same behaviour. Here, again, the flow field was dominated

https://doi.org/10.1017/jfm.2014.371 Published online by Cambridge University Press

by a strong $(\gamma_1, 2)$ inertial wave that was superimposed by several higher harmonics. All experiments revealed a clear manifestation of the wave structures in the central domain of the cylinder, where the Ekman-driven recirculation tori of the secondary flow and turbulent fluctuations dominate the outer region at larger radii.

Acknowledgements

The authors are very grateful to K. Eckert and E. Kaplan for fruitful discussions and critical reading of the manuscript. Moreover, we would like to thank the anonymous reviewers for their valuable suggestions and comments. This work was supported by the German Science Foundation (DFG) in the framework of the Collaborative Research Centre SFB609 'Electromagnetic Flow Control in Metallurgy, Crystal Growth and Electrochemistry'.

REFERENCES

ALDRIDGE, K. D. & LUMB, L. I. 1987 Inertial waves identified in the Earth's fluid outer core. *Nature* **325**, 421–423.

BARUTEAU, C. & RIEUTORD, M. 2013 Inertial waves in a differentially rotating spherical shell. *J. Fluid Mech.* **719**, 47–81.

BJERKNES, V. & SOLBERG, H. 1929 Zellulare Trägheitswellen und Turbulenz. *Avhandl. Norske Vid. Akad. Mat. Nat* (7), 1–16.

BRITO, D., NATAF, H. C., CARDIN, P., AUBERT, J. & MASSON, J. P. 2001 Ultrasonic Doppler velocimetry in liquid gallium. *Exp. Fluids* **31** (6), 653–663.

DAVIDSON, P. A. 1992 Swirling flow in an axisymmetric cavity of arbitrary profile, driven by a rotating magnetic field. *J. Fluid Mech.* **245**, 669–699.

DAVIDSON, P. A. & HUNT, J. C. R. 1987 Swirling recirculating flow an a liquid-metal column generated by a rotating magnetic field. *J. Fluid Mech.* **185**, 67–106.

ECKERT, S. & GERBETH, G. 2002 Velocity measurements in liquid sodium by means of ultrasound Doppler velocimetry. *Exp. Fluids* **32** (5), 542–546.

ECKERT, S., NIKRITYUK, P., RÄBIGER, D., ECKERT, K. & GERBETH, G. 2007 Efficient melt stirring using pulse sequences of a rotating magnetic field: part I. Flow field in a liquid metal column. *Metall. Mater. Trans.* B **38** (6), 977–988.

FU, L. L. 1980 Observations and models of inertial waves in the deep ocean. PhD thesis, Massachusetts Institute of Technology and Woods Hole Oceanographic Institution.

FULTZ, D. 1959 A note on overstability and the elastoid-inertia oscillations of Kelvin, Solberg, and Bjerknes. *J. Atmos. Sci.* **16**, 199–208.

GAILITIS, A., LIELAUSIS, O., PLATACIS, E., DEMENT'EV, S., CIFERSONS, A., GERBETH, G., GUNDRUM, T., STEFANI, F., CHRISTEN, M. & WILL, G. 2001 Magnetic field saturation in the Riga dynamo experiment. *Phys. Rev. Lett.* **86** (14), 3024–3027.

GORBACHEV, L. P., NIKITIN, N. V. & USTINOV, A. L. 1974 Magnetohydrodynamic rotation of electrically conducting liquid in a cylindrical vessel of finite dimensions. *Magn. Gidrodin.* (4), 32–42.

GÖRTLER, H. 1957 On forced oscillations in rotating fluids. In *Proceedings of the 5th Midwestern Conference on Fluid Mechanics*, pp. 1–10.

GRANTS, I. & GERBETH, G. 2001 Stability of axially symmetric flow driven by a rotating magnetic field in a cylindrical cavity. *J. Fluid Mech.* **431**, 407–426.

GRANTS, I. & GERBETH, G. 2002 Linear three-dimensional instability of a magnetically driven rotating flow. *J. Fluid Mech.* **463**, 229–239.

GRANTS, I., ZHANG, C., ECKERT, S. & GERBETH, G. 2008 Experimental observation of swirl accumulation in a magnetically driven flow. *J. Fluid Mech.* **616**, 135–152.

GREENSPAN, H. P. 1968 *The Theory of Rotating Fluids*. Cambridge University Press.

https://doi.org/10.1017/jfm.2014.371 Published online by Cambridge University Press

GRIFFITHS, W. D. & MCCARTNEY, D. G. 1996 The effect of electromagnetic stirring during solidification on the structure of Al–Si alloys. *Mater. Sci. Engng* A **216**, 47–60.

HOLLERBACH, R. & KERSWELL, R. R. 1995 Oscillatory inertial shear layer in rotating and precessing flows. *J. Fluid Mech.* **298**, 327–339.

KELLEY, D. H., TRIANA, S. A., ZIMMERMAN, D. S. & LATHROP, D. P. 2010 Selection of inertial modes in spherical Couette flow. *Phys. Rev.* E **81**, 026311.

KELLEY, D. H., TRIANA, S. A., ZIMMERMAN, D. S., TILGNER, A. & LATHROP, D. P. 2007 Inertial waves driven by differential rotation in a planetary geometry. *Geophys. Astrophys. Fluid Dyn.* **101**, 469–487.

KELVIN, LORD 1880 Vibrations of a columnar vortex. *Phil. Mag.* **10** (5), 155–168.

KOBINE, J. J. 1995 Inertial wave dynamics in a rotating and precessing cylinder. *J. Fluid Mech.* **303**, 233–252.

MANASSEH, R. 1992 Breakdown regimes of inertial waves in a precessing cylinder. *J. Fluid Mech.* **243**, 261–296.

MESSIO, L., MORIZE, C., RAUBAUD, M. & MOISY, F. 2008 Experimental observation using particle image velocimetry of inertial waves in a rotating fluid. *Exp. Fluids* **44** (1), 519–528.

MONCHAUX, R., BERHANU, M., BOURGOIN, M., MOULIN, M., ODIER, P., PINTON, J.-F., VOLK, R., FAUVE, S., MORDANT, N., PÉTRÉLIS, F., CHIFFAUDEL, A., DAVIAUD, F., DUBRULLE, B., GASQUET, C., MARIÉ, L. & RAVELET, F. 2007 Generation of a magnetic field by dynamo action in a turbulent flow of liquid sodium. *Phys. Rev. Lett.* **98**, 044502.

NATAF, H.-C., ALBOUSSIÈRE, T., BRITO, D., CARDIN, P., GAGNIÈRE, N., JAULT, D., MASSON, J.-P. & SCHMITT, D. 2006 Experimental study of super-rotation in a magnetostrophic spherical Couette flow. *Geophys. Astrophys. Fluid Dyn.* **100**, 281–298.

NIKRITYUK, P. A., UNGARISH, M., ECKERT, K. & GRUNDMANN, R. 2005 Spin-up of a liquid metal flow driven by a rotating magnetic field in a finite cylinder: a numerical and an analytical study. *Phys. Fluids* **17**, 067101.

PAL, J., CRAMER, A., GUNDRUM, T. & GERBETH, G. 2009 MULTIMAG, a multipurpose magnetic system for physical modelling in magnetohydrodynamics. *Flow Meas. Instrum.* **20** (6), 241–251.

RÄBIGER, D., ECKERT, S. & GERBETH, G. 2010 Measurements of an unsteady liquid metal flow during spin-up driven by a rotating magnetic field. *Exp. Fluids* **48** (2), 233–244.

RÄBIGER, D., ECKERT, S., GERBETH, G., CZARSKE, J. & FRANKE, S. 2012 Flow structures arising from melt stirring by means of modulated rotating magnetic fields. *Magnetohydrodynamics* **48** (1), 213–220.

RAYLEIGH, LORD 1917 On the dynamics of revolving fluids. *Proc. R. Soc. Lond.* A **93** (648), 148–154.

SAURET, A., CÉBRON, D., LE BARS, M. & LE DIZÈS, S. 2005 Fluid flows in a librating cylinder. *Phys. Fluids* **24**, 026603.

SCHMITT, D., ALBOUSSIRE, T., BRITO, D., CARDIN, P., GAGNIERE, N., JAULT, D. & NATAF, H.-C. 2008 Rotating spherical Couette flow in a dipolar magnetic field: experimental study of magneto-inertial waves. *J. Fluid Mech.* **604**, 175–197.

STEFANI, F., GUNDRUM, T., GERBETH, G., RÜDIGER, G., SCHULTZ, M., SZKLARSKI, J. & HOLLERBACH, R. 2006 Experimental evidence for magnetorotational instability in a Taylor–Couette flow under the influence of a helical magnetic field. *Phys. Rev. Lett.* **97** (18), 184502.

STIEGLITZ, R. & MÜLLER, U. 2001 Experimental demonstration of a homogeneous two-scale dynamo. *Phys. Fluids* **13**, 561–564.

STILLER, J., FRAŇA, K. & CRAMER, A. 2006 Transitional and weakly turbulent flow in a rotating magnetic field. *Phys. Fluids* **18**, 074105.

TACKE, K. H. & SCHWERDTFEGER, K. 1979 Rührgeschwindigkeit in Rundstrangguss bei Rührung mit elektromagnetischen Drehfeldern. *Stahl Eisen.* **99** (1), 7–12.

TAKEDA, Y. 1991 Development of an ultrasound velocity profile monitor. *Nucl. Engng Des.* **126** (2), 277–284.

THOMPSON, R. 1978 Observation of inertial waves in the stratosphere. *Q. J. R. Meteorol. Soc.* **104** (441), 691–698.

https://doi.org/10.1017/jfm.2014.371 Published online by Cambridge University Press

VOGT, T., GRANTS, I., RÄBIGER, D., ECKERT, S. & GERBETH, G. 2012 On the formation of Taylor–Görtler vortices in RMF-driven spin-up flows. *Exp. Fluids* **52** (1), 1–10.

VOGT, T., GRANTS, I., ECKERT, S. & GERBETH, G. 2013 Spin-up of a magnetically driven tornado-like vortex. *J. Fluid Mech.* **736**, 641–662.

ZHANG, C., SHATROV, V., PRIEDE, J., ECKERT, S. & GERBETH, G. 2011 Intermittent behavior caused by surface oxidation in a liquid metal flow driven by a rotating magnetic field. *Metall. Mater. Trans.* B **42** (6), 1188–1200.

https://doi.org/10.1017/jfm.2014.371 Published online by Cambridge University Press